

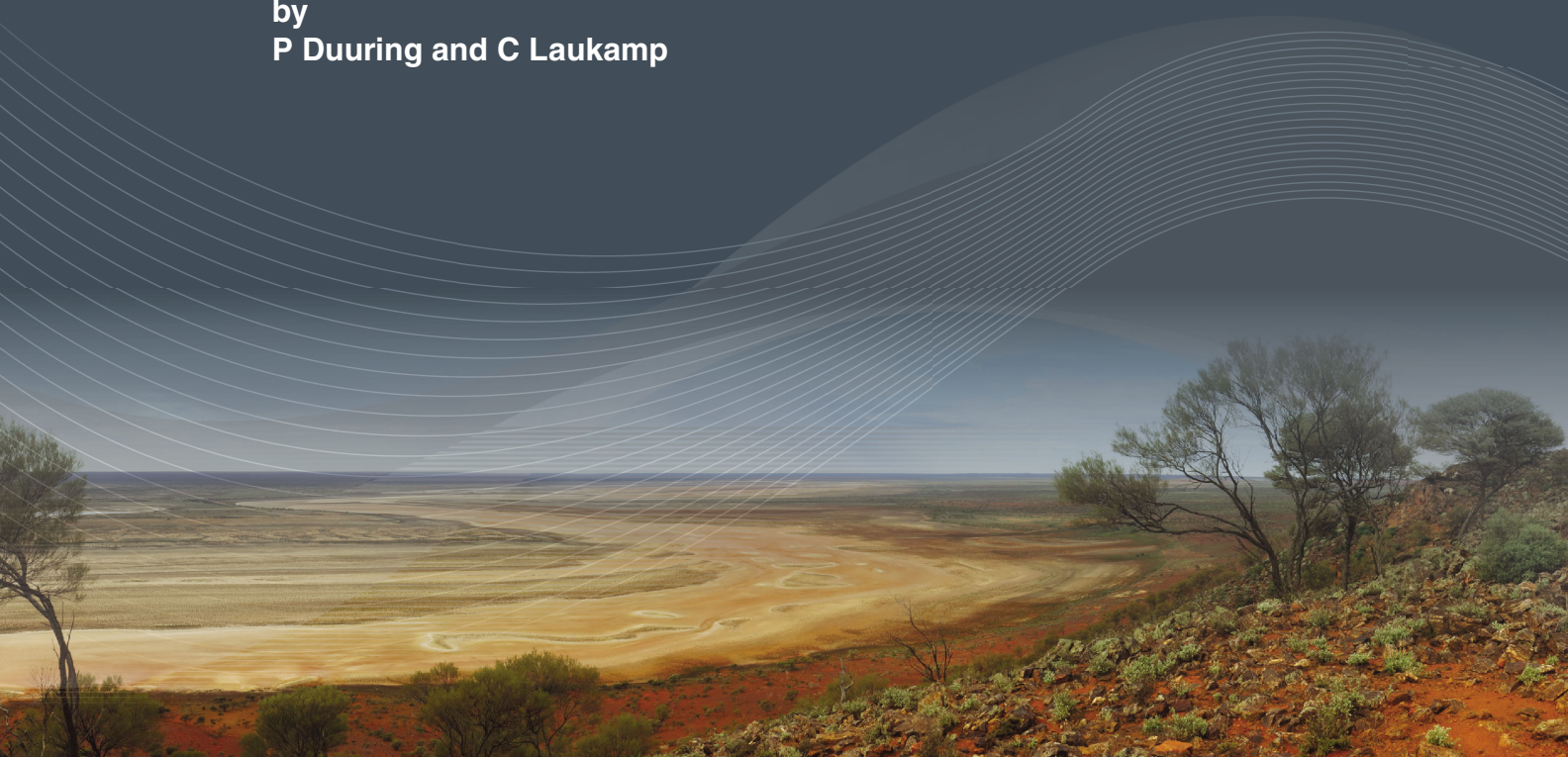


Government of Western Australia  
Department of Mines and Petroleum

RECORD 2016/17

# MAPPING IRON ORE ALTERATION PATTERNS IN BANDED IRON-FORMATION USING HYPERSENSITIVE DATA: WINDARLING IRON CAMP, YILGARN CRATON, WESTERN AUSTRALIA

by  
P Duuring and C Laukamp



Geological Survey of  
Western Australia



EXPLORATION  
INCENTIVE SCHEME

Centre for EXPLORATION  
TARGETING





Government of **Western Australia**  
Department of **Mines and Petroleum**

**Record 2016/17**

# **MAPPING IRON ORE ALTERATION PATTERNS IN BANDED IRON-FORMATION USING HYPERSPECTRAL DATA: WINDARLING IRON CAMP, YILGARN CRATON, WESTERN AUSTRALIA**

by

**P Duuring and C Laukamp<sup>1</sup>**

<sup>1</sup> Western Australian Centre of Excellence for 3D Mineral Mapping, CSIRO Mineral Resources, 26 Dick Perry Avenue, Kensington WA 6151

**Perth 2016**



**Geological Survey of  
Western Australia**

**MINISTER FOR MINES AND PETROLEUM**  
**Hon. Sean K L'Estrange MLA**

**ACTING DIRECTOR GENERAL, DEPARTMENT OF MINES AND PETROLEUM**  
**Tim Griffin**

**EXECUTIVE DIRECTOR, GEOLOGICAL SURVEY OF WESTERN AUSTRALIA**  
**Rick Rogerson**

#### **REFERENCE**

**The recommended reference for this publication is:**

Duuring P and Laukamp C 2016, Mapping iron ore alteration patterns in banded iron-formation using hyperspectral data: Windarling iron camp, Yilgarn Craton, Western Australia: Geological Survey of Western Australia, Record 2016/17, 14p.

**National Library of Australia Card Number and ISBN 978-1-74168-722-4**

Grid references in this publication refer to the Geocentric Datum of Australia 1994 (GDA94). Locations mentioned in the text are referenced using Map Grid Australia (MGA) coordinates, Zone 50. All locations are quoted to at least the nearest 100 m.



#### **Disclaimer**

This product was produced using information from various sources. The Department of Mines and Petroleum (DMP) and the State cannot guarantee the accuracy, currency or completeness of the information. DMP and the State accept no responsibility and disclaim all liability for any loss, damage or costs incurred as a result of any use of or reliance whether wholly or in part upon the information provided in this publication or incorporated into it by reference.

#### **Published 2016 by Geological Survey of Western Australia**

This Record is published in digital format (PDF) and is available online at <[www.dmp.wa.gov.au/GSWApublications](http://www.dmp.wa.gov.au/GSWApublications)>.

#### **Further details of geological products and maps produced by the Geological Survey of Western Australia are available from:**

Information Centre  
Department of Mines and Petroleum  
100 Plain Street  
EAST PERTH WESTERN AUSTRALIA 6004  
Telephone: +61 8 9222 3459 Facsimile: +61 8 9222 3444  
[www.dmp.wa.gov.au/GSWApublications](http://www.dmp.wa.gov.au/GSWApublications)

**Cover image:** Elongate salt lake on the Yilgarn Craton — part of the Moore–Monger paleovalley — here viewed from the top of Wownaminy Hill, 20 km southeast of Yalgoo, Murchison Goldfields. Photograph taken by I Zibra for the Geological Survey of Western Australia

## Contents

Abstract .....	1
Introduction.....	1
Geological overview of the W2 deposit .....	1
Results from conventional logging of diamond drillhole W2DDH007 .....	4
Rock types.....	4
Hypogene alteration of BIF.....	7
Hypogene alteration of mafic igneous rocks.....	7
Supergene alteration of BIF .....	7
Supergene alteration of mafic igneous rocks .....	7
Results of hyperspectral data acquisition and processing .....	7
Method .....	7
Rock types.....	8
Hypogene alteration zones in BIF.....	8
Hypogene alteration zones in mafic igneous rocks .....	9
Supergene alteration zones in BIF .....	9
Supergene alteration of mafic igneous rocks .....	9
Conclusions.....	11
Acknowledgements .....	13
References .....	13

## Appendix

Description of spectral scripts for geoscience products .....	14
---	----

## Figures

1. Iron ore occurrences in the Yilgarn Craton and location of diamond drillhole W2DDH007.....	2
2. Solid geology map of the Windarling iron camp .....	3
3. Geology map and cross section of the W2 deposit, with location of drillhole W2DDH007 .....	4
4. Summary log for drillhole W2DDH007 showing hyperspectral data .....	5
5. Immobile element ratios for mafic igneous rocks .....	9
6. Hyperspectral data for BIF macrobands: opaque mineral abundance data .....	10
7. Hyperspectral data for BIF macrobands: chlorite abundance vs chemistry .....	11
8. Hyperspectral data for mafic igneous rocks: chlorite abundance vs chemistry .....	12





# Mapping iron ore alteration patterns in banded iron-formation using hyperspectral data: Windarling iron camp, Yilgarn Craton, Western Australia

by

P Duuring and C Laukamp<sup>1</sup>

## Abstract

Core from the W2DDH007 diamond drillhole, located in the W2 deposit of the Windarling iron camp, was scanned using the HyLogger-3 at GSWA's Perth Core library to identify hypogene alteration mineral vectors for high-grade iron ore hosted by banded iron-formation (BIF). Drillhole W2DDH007 intersects four well-mineralized BIF macrobands that are surrounded by basalt. All rocks are fresh to weakly weathered. The 'ferric oxide abundance' spectral product accurately distinguishes BIF from basalt because high spectral signature corresponds to a high abundance of hematite in BIF. However, this spectral product is less effective in weathered zones because hematite and goethite are likely to be present in supergene-altered mafic rocks. The 'chlorite abundance' and 'chlorite-epidote abundance' spectral products were highly effective at identifying basalt intervals. The 'amphibole-talc', 'amphibole', 'plagioclase', 'serpentine', and 'epidote' abundance products were only locally useful for identifying mafic igneous rocks. High-grade, hypogene magnetite  $\pm$  specular hematite-rich ore zones in BIF show a major decrease in the 'quartz abundance' product relative to areas of least-altered BIF. These intervals display a matching increase in the detected presence of siderite (using the TIR spectrometer). The ferric oxide abundance index identifies intervals of BIF that are rich in specular hematite, whereas coincident elevated chlorite abundance signatures confirm the cogenetic relationship between these minerals. The chemistry of chlorite in these areas of BIF varies between the Fe- to Mg-rich end member compositions. Proximal hypogene alteration zones in mafic igneous rocks are strongly enriched in hypogene chlorite and depleted in igneous amphibole, compared to mafic rocks located distal to contacts with magnetite  $\pm$  specular hematite-rich ore zones hosted in BIF. The chemistry of hypogene chlorite becomes increasingly Fe rich with proximity to BIF-hosted hypogene iron ore zones.

**KEYWORDS:** banded iron-formation, hypogene deposits, iron ores, spectral analysis, supergene alteration

## Introduction

Reflectance spectral data were collected by the HyLogger-3 for six diamond drillholes from four iron ore deposits located in various greenstone belts throughout the Yilgarn Craton. The sites of interest include the Weld Range (drillhole WRRD0583; Duuring and Laukamp, 2016a), Koolyanobbing, Mt Richardson (Duuring and Laukamp, 2016b,c), and Windarling (this study) iron camps (Fig. 1). The aim is to identify hypogene and supergene alteration minerals associated with high-grade iron ore ( $>57$  wt% Fe<sub>total</sub>) in banded iron-formation (BIF) and nearby mafic country rocks. For this purpose, reflectance spectral data were collected by the HyLogger-3 for core from diamond drillhole W2DDH007, which

intersects high-grade iron ore hosted by BIF at the W2 deposit in the Windarling iron camp (Figs 1, 2). This report presents the acquired reflectance spectra and interprets the data.

## Geological overview of the W2 deposit

The geology of the W2 deposit was documented in detail by Angerer et al. (2013); a summary of that work is given here. High-grade iron ore deposits hosted by BIF in the Windarling iron camp are located within the 3050–2930 Ma lower greenstone succession of the Marda–Diemals greenstone belt, Southern Cross Domain (Cassidy et al., 2006). The iron camp includes several deposits (e.g. the W1, W2, W3, W4, W6, W7, and W10) distributed across multiple, 10–50 m thick, BIF macrobands separated by high-Mg basalt flows (Fig. 2).

---

<sup>1</sup> Western Australian Centre of Excellence for 3D Mineral Mapping, CSIRO Mineral Resources, 26 Dick Perry Avenue, Kensington WA 6151

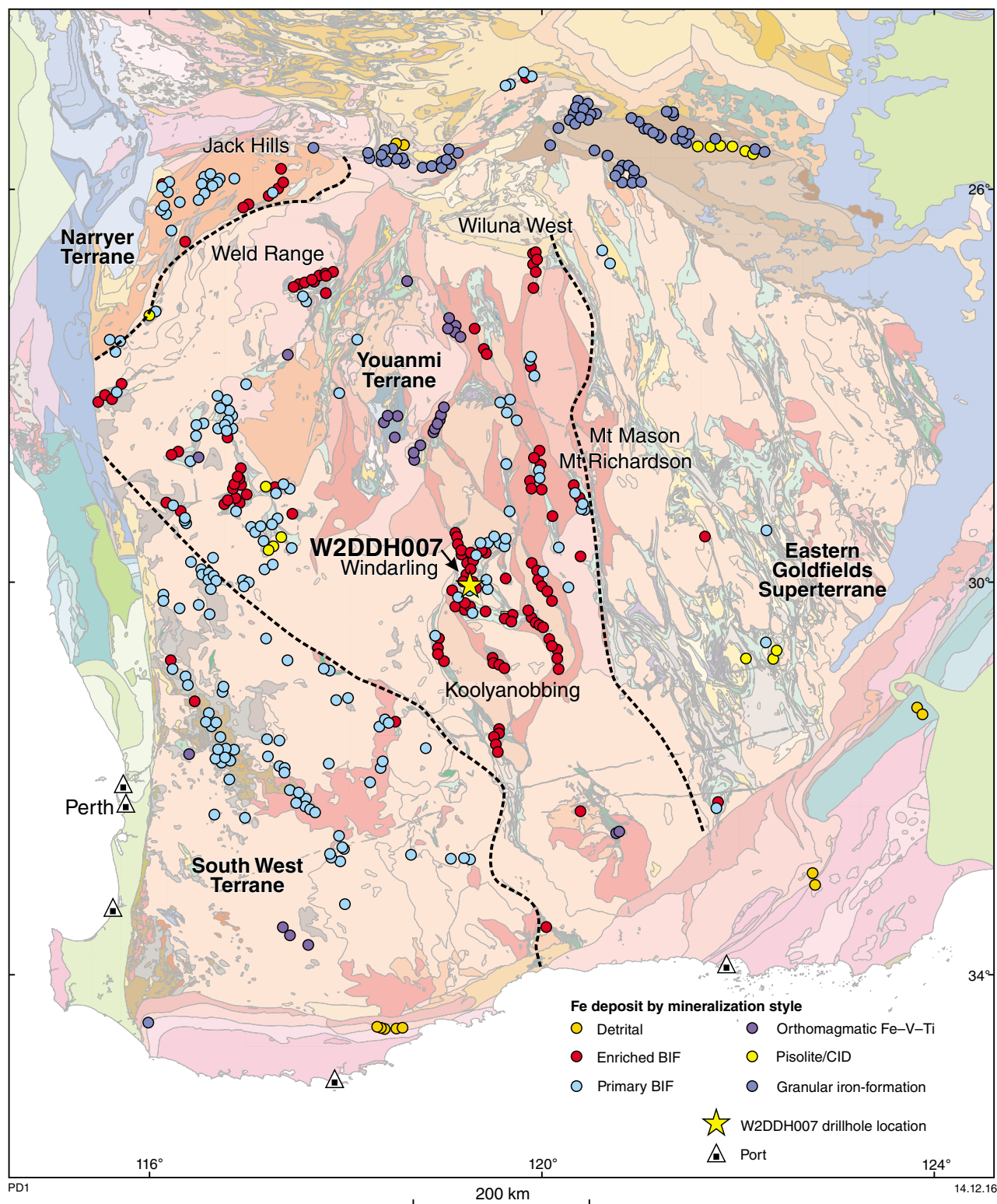
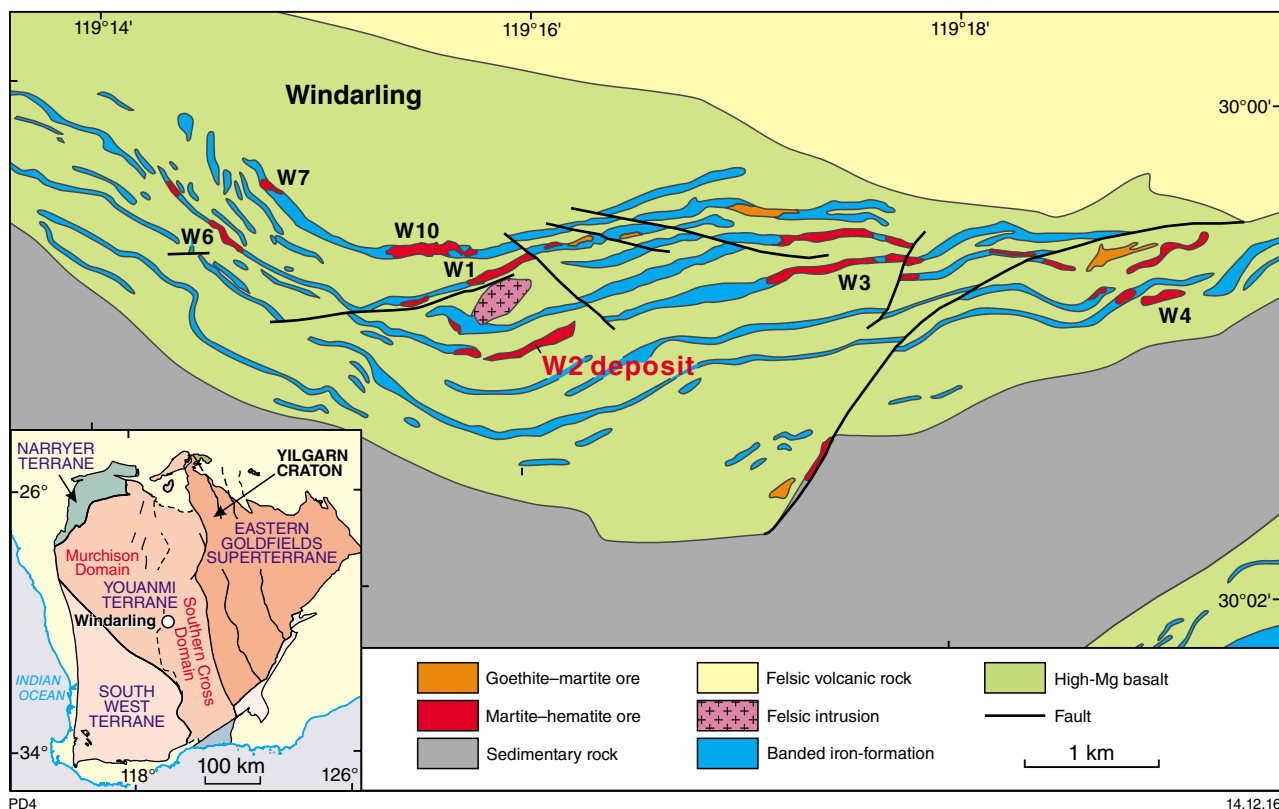


Figure 1. Distribution of iron ore occurrences in the Yilgarn Craton and location of diamond drillhole W2DDH007 in the Windarling iron camp. Regional geological map from GSWA (2016); iron ore deposits from the GSWA MINEDEX database <[www.dmp.wa.gov.au/minedex](http://www.dmp.wa.gov.au/minedex)>. CID – channel iron deposit



**Figure 2. Solid geology map of the Windarling iron camp, showing the distribution of rock types, structures, and known iron ore deposits W1 to W4, W6, W7, and W10 (modified after Angerer et al., 2013)**

All rocks are metamorphosed to lower-greenschist facies. The dominant ore type in BIF is martite–hematite–goethite ore, with examples of magnetite–hematite ore located beneath the weathering zone. The combined resource for the Windarling iron camp is at least 52 Mt at 60 wt% Fe<sub>total</sub> (Angerer et al., 2013 and references cited therein).

The W2 deposit is located in the centre of the Windarling iron ore camp (Fig. 2). At W2, BIF-hosted iron ore bodies strike east–west and extend for about 1 km along strike (Fig. 3a). The dominant ore type is magnetite–hematite–martite–goethite associated with four steeply south-dipping BIF bands, labelled BIF1 to BIF4 from south to north in the deposit and with increasing depth in hole W2DDH007 (Fig. 3b; Angerer et al., 2013). High-grade magnetite–hematite ore is hosted by all four BIF macrobands below the weathering front at 70 m depth in this hole. A small felsic intrusion is exposed about 500 m north of W2 (Fig. 2).

Least-altered BIF in W2DDH007 comprises cryptocrystalline hematite, quartz, and magnetite (i.e. a jaspilite; Angerer et al., 2013). High-grade magnetite–hematite ore zones are surrounded by hypogene carbonate alteration haloes in unweathered BIF, whereby the carbonate minerals replace primary silica-rich bands. Neighbouring, unweathered and least-altered, high-MgO basalts are massive, light to dark green, fine to medium grained, and locally display a weak schistosity

defined by chlorite along the sheared margins of BIF macrobands. The basaltic rocks mainly comprise chlorite (80 vol%) and epidote (5 vol%), which replace primary plagioclase, olivine, pyroxene, and amphibole. Primary (titano-)magnetite phenocrysts are mostly replaced by leucoxene. Specular hematite – quartz – dolomite veins are locally present in the hanging wall to the BIF1 macroband, whereas ferroan calcite – quartz veins occur in the footwall to BIF4 (Fig. 3b; Angerer et al., 2013). In addition, quartz – dolomite – specular hematite veins cut BIF macrobands, whereas chlorite–magnetite–pyrite veins are common in areas proximal to BIF macrobands. Weathered mafic rocks occur from the surface to depths of about 80 m and the basalt comprises cryptocrystalline hematite, goethite, and kaolinite.

Three main hypogene alteration stages are recorded by BIF at the Windarling W2 deposit. Stage 1 hypogene alteration was structurally controlled by the fault reactivation of BIF–basalt margins and crosscutting faults. Circulating hydrothermal fluids resulted in the replacement of primary silica-rich bands in BIF by ferroan dolomite and magnetite, with associated depletion in SiO<sub>2</sub> and enrichments in Fe<sub>total</sub>, CaO, MgO, MnO, Ni, Co, P<sub>2</sub>O<sub>5</sub>, and rare earth elements (REE). Surrounding basalts were most likely the main source of MgO, CaO, Ni, and Co, whereas P<sub>2</sub>O<sub>5</sub> and REE may have been derived from more distal granites (Angerer et al., 2013).

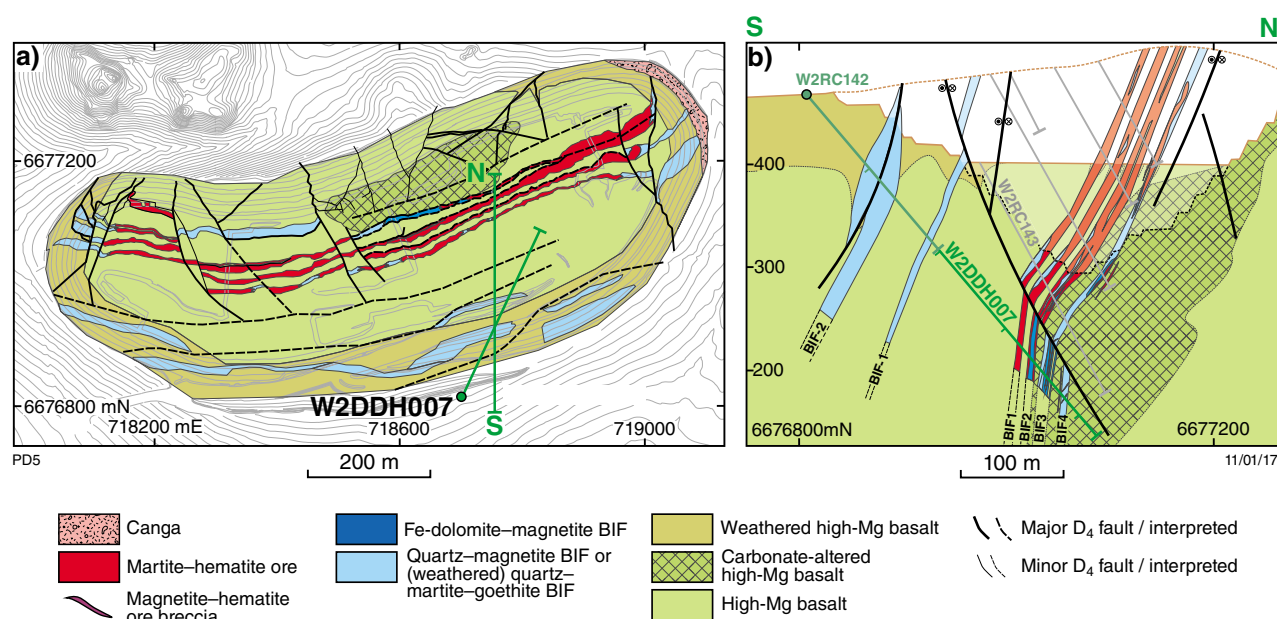


**Figure 3. Geology of the W2 deposit and location of drillhole W2DDH007: a) plan view; b) cross-section (modified after Angerer et al., 2013). Trace of the drillhole has been projected into the cross-section line.**

During Stage 2 alteration, an acidic and oxidized fluid flowed along reactivated BIF margins and within first-generation faults, resulting in the leaching of ferroan dolomite, significant volume reduction and concentration of residual magnetite–martite, and the local precipitation of minor lepidoblastic and anhedral granoblastic hematite. The resultant magnetite–hematite(–martite) ores are strongly enriched in  $\text{Fe}_{\text{total}}$  and depleted in  $\text{SiO}_2$  relative to least-altered BIF.

Stage 3 alteration involved the development of specular hematite – ferroan dolomite – quartz veins and wallrock alteration zones. Stage 4 alteration involved Mesozoic to recent supergene oxidation and hydration of BIF to depths of about 200 m below the present surface. During this event, existing dolomite and quartz in BIF were replaced by goethite, whereas magnetite was replaced by martite. The corresponding goethite–martite ore is strongly depleted in  $\text{SiO}_2$ ,  $\text{MgO}$ ,  $\text{CaO}$ ,  $\text{MnO}$ ,  $\text{K}_2\text{O}$ , and  $\text{Na}_2\text{O}$ , whereas  $\text{Fe}_{\text{total}}$  and  $\text{P}_2\text{O}_5$  are enriched relative to least-altered BIF (Angerer et al., 2013). (Ca,Mg)-carbonate alteration in proximal mafic rocks is considered by Angerer et al. (2013) to be a predictive exploration vector for hypogene iron ore hosted by BIF. The geochemical ratio  $(\text{CaO}+\text{MgO}+\text{MnO})/\text{Fe}_2\text{O}_3$  vs  $\text{SiO}_2/\text{Fe}_2\text{O}_3$  is a useful discriminator of least-altered BIF, carbonate-altered BIF, and high-grade iron ore zones (Angerer et al., 2013).

## Results from conventional logging of diamond drillhole W2DDH007

Hole W2DDH007 was drilled from the surface (MGA 718699E 6676810N) at an angle of  $-50^\circ$  towards  $025^\circ$  for

a total length of 428 m. This diamond drillhole was chosen because it intersects unweathered examples of high-Mg basalt, four BIF macrobands, and high-grade magnetite–martite–hematite ore (57–68 wt%  $\text{Fe}_{\text{total}}$ ). Basalt footwall and hangingwall rock to BIF displays mineralogical and textural zonation away from ore zones. Unless otherwise stated, provided depth measurements are in reference to the depth down the inclined hole rather than vertical depths from the present surface.

The first 202 m was drilled by the reverse circulation method, but the resultant rock chips were not available for study. Instead, diamond drillcore from the interval 202–428 m was transported to Perth and scanned using the HyLogger-3 at the Geological Survey of Western Australia (GSWA) in May 2013. The diamond drillcore was logged by conventional means, which included the documentation of relationships between rock types, textures, structures, and hypogene alteration mineral assemblages, and comparison with bulk-rock geochemical data. Drillhole W2DDH007 was returned to the Windarling mine site in April 2014.

## Rock types

Four BIF macrobands, labelled BIF1 to BIF4 with increasing depth, are enveloped by high-Mg basalt in drillhole W2DDH007 (Fig. 4). The BIF macrobands vary in individual thickness from 8–15 m and are separated by basalt intervals (Mafic2, Mafic3, Mafic4) that are 9–18 m thick. Least-altered high-Mg basalt is located on either side of the suite of BIF macrobands, and is labelled Mafic1 and Mafic5 with increasing depth (Fig. 4). These mafic igneous rocks are dark green, massive, and fine to medium grained (1–3 mm grain size), and comprise primary igneous plagioclase, pyroxene, amphibole, and minor



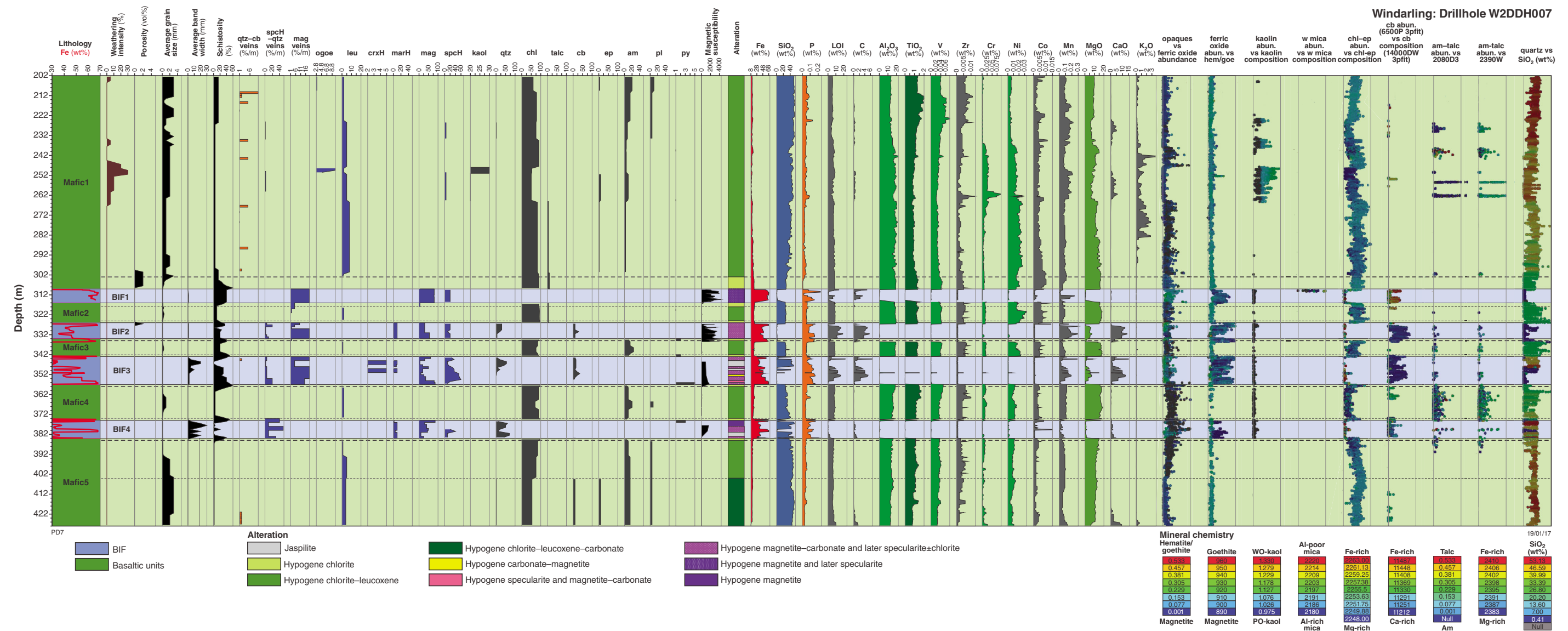


Figure 4. Hyperspectral log for W2DDH007. Abbreviations: abund – abundance; am – amphibole; cb – carbonate; chl – chlorite; crxH – crystalline hematite; ep – epidote; ferric oxide – ferric oxide minerals; goe – goethite; kaol – kaolinite; leu – leucoxene; LOI – loss on ignition; mag – magnetite; marH – martite; ogoe – ochreous goethite; opaques – opaque minerals; pl – plagioclase; py – pyrite; PO-kaol – poorly ordered kaolinite; qtz – quartz; spcH – specular hematite; vgoe – vitreous goethite; w mica – white mica; WO-kaol – well-ordered kaolinite

disseminated magnetite. These minerals are locally replaced by metamorphic chlorite, epidote, ilmenite, and leucoxene. Mafic igneous units are interpreted to be extrusive flows located between BIF macrobands (Angerer et al., 2013).

Examples of least-altered BIF (i.e. jaspilite) are present in the BIF3 (345–348 m) and BIF4 (381–383 m) macrobands. Here, the rock is pale red and comprises alternating, 0.5 – 2 cm thick, silica- and iron oxide-rich bands. The silica-rich (jasper) bands contain very fine-grained quartz with disseminated cryptocrystalline hematite. The iron oxide bands comprise a mix of primary magnetite(–martite) and hypogene crystalline hematite (microplaty to specular). Least-altered BIF is rich in  $\text{SiO}_2$  (42.44 – 50.28 wt%) and  $\text{Fe}_{\text{total}}$  (32.10 – 38.88 wt%), with minor  $\text{P}_2\text{O}_5$  (0.061 – 0.124 wt%), LOI content (0.26 – 0.90 wt%), C (0.38 – 0.65 wt%), Co (<0.001 wt%), and MnO (<0.03 wt%).

## Hypogene alteration of BIF

Of the BIF macrobands intersected, the 7 m thick, dark grey to black and massive to weakly banded BIF1 macroband (309–316 m) is the most intensively and pervasively altered. These alteration zones are rich in martite, as well as hypogene magnetite, specularite and microplaty hematite. The primary martite bands and later hypogene magnetite are moderately overprinted by hypogene crystalline hematite and chlorite. The interval displays uniformly high  $\text{Fe}_{\text{total}}$  values (57–68 wt%) with low  $\text{SiO}_2$  (0.68 – 2.50 wt%), indicating the replacement of primary jasper bands by hypogene magnetite and then hematite. The hypogene magnetite ( $\pm$  specularite) alteration zone contains narrower zones (e.g. from 312 to 313 m) of elevated  $\text{P}_2\text{O}_5$  (0.068 – 0.118 wt%), LOI content (5.64 – 8.36 wt%), C (2.29 – 3.14 wt%), Co (0.002 – 0.003 wt%), and MnO (0.22 – 0.31 wt%). The spatial association between elevated LOI, C, and  $\text{P}_2\text{O}_5$  values suggests the presence of carbonate and phosphate minerals, whereas the anomalous Co and MnO likely indicates fluid flow resulting in chemical exchange with neighbouring mafic igneous rocks.

The BIF2, BIF3, and BIF4 macrobands contain narrow (1–2 m thick) zones of high-grade iron ore, mainly located along the margins of the respective macrobands (Fig. 4). BIF4 also contains a 2 m thick, high-grade iron ore zone located in the middle of the macroband (i.e. from 379 to 381 m). These alteration zones are dominated by hypogene magnetite  $\pm$  carbonate with a moderate overprint by hypogene crystalline hematite  $\pm$  chlorite  $\pm$  pyrite. Magnetite veins and later specularite–quartz veins locally cut the primary bands in BIF, whereas quartz–carbonate veins cut all rock types and other vein types. Relative to least-altered BIF, the unweathered and hypogene-altered BIF2, BIF3, and BIF4 macrobands display highly variable depletions in  $\text{SiO}_2$  (–0.81 – 42.82 wt%) and enrichments in  $\text{Fe}_{\text{total}}$  (21.15 – 66.91 wt%),  $\text{P}_2\text{O}_5$  (0.086 – 0.109 wt%), LOI content (<22.12 wt%), C (0.20 – 6.67 wt%), CaO (0.70 – 13.88 wt%), MgO (0.52 – 7.48 wt%), and MnO (0.03 – 0.37 wt%), with local enrichments in Co (<0.003 wt%), S (<0.18 wt%), Cu (<0.14 wt%), Au (<8.5 ppb), and U (<0.2 ppm) (Fig. 4).

## Hypogene alteration of mafic igneous rocks

Proximal alteration zones in unweathered basaltic rocks are located along the margins of BIF macrobands (Fig. 4). The widest observed proximal alteration zone borders the upper contact of BIF1 (i.e. from 301 to 309 m); the proximal zone is at least 9 m thick and is finer grained compared with more distal rocks. Hypogene chlorite replaces primary amphibole and pyroxene. Metamorphic leucoxene is notably absent in this interval. The other BIF margins also display proximal alteration zones in mafic igneous rocks, but they are narrower (1–2 m thick). Relative to more distal examples of unweathered mafic igneous rocks (e.g. at 202 m), the proximal zones are uniformly enriched in  $\text{Fe}_{\text{total}}$  (i.e. an increase from 12.30 to 19.50 wt%), Co (from 0.003 to 0.010 wt%), MgO (from 9.80 to 16.60 wt%), and are locally enriched in S (<0.235 wt%), Cu (<0.153 wt%), Zn (<0.015 wt%), Au (<2.6 ppb), and U (<0.6 ppm). These proximal zones are uniformly depleted in  $\text{SiO}_2$  (from 50.31 to 26.36 wt%),  $\text{P}_2\text{O}_5$  (from 0.057 to 0.007 wt%), and  $\text{K}_2\text{O}$  (from 0.47 to 0.01 wt%; Fig. 4). The width of the proximal alteration zones in mafic rocks appears to be proportional to the width and intensity of hypogene alteration zones in BIF; specifically, alteration widths are greatest in mafic igneous rocks adjacent to BIF1.

## Supergene alteration of BIF

Supergene alteration is negligible in BIF in drillhole W2DDH007.

## Supergene alteration of mafic igneous rocks

Weak to moderate supergene alteration is exhibited by high-Mg basalt from about 245–265 m. In this interval of core, primary igneous amphibole, pyroxene, olivine and plagioclase, and metamorphic epidote and chlorite, are replaced by ochreous goethite, cryptocrystalline hematite, and kaolinite. Weakly to moderately altered mafic igneous rocks display local enrichment in Cr (from 0.002 to 0.091 wt%) and MnO (from 0.14 to 0.18 wt%), and depletion in MgO (from 9.80 to 7.45 wt%; Fig. 4).

## Results of hyperspectral data acquisition and processing

### Method

A detailed description of the general principles of the HyLogger-3 is provided by Hancock et al. (2013) and Duuring and Laukamp (2016a). The HyLogger-3 hyperspectral scanning system developed by CSIRO in Australia uses reflectance spectra of scanned diamond drillcore to identify mineral abundances and mineral chemistry (Hunt, 1977; Clark and Roush, 1984). The

HyLogger-3 operated by GSWA in Perth detects radiation reflected from the drillcore within the visible to near infrared (VNIR, 380–1000 nm), short wave infrared (SWIR, 1000–2500 nm) and thermal infrared (TIR, 6000–14000 nm) parts of the electromagnetic spectrum. The HyLogger-3 uses an automated x–y table that moves the core tray at intervals of 1 cm data resolution (Haest et al., 2012a). The reflectance spectra are cross-calibrated using a Spectralon panel. During the nondestructive scanning process, the HyLogger-3 also captures high-resolution digital core images, which are referenced to a standard set of Munsell colours. The hyperspectral data are then processed to determine the abundance of minerals, as well as their composition and/or crystallinity, based on the wavelength, depth and width of diagnostic absorption features. Algorithms applied in this project were developed by CSIRO (Laukamp, 2011; Haest et al., 2012a; Sonntag et al., 2012) and were used in this study to determine mineral abundance and composition of iron oxides, including hematite, vitreous goethite and ochreous goethite, and other minerals such as chlorites, carbonates, amphiboles, white micas, and kaolin group minerals (Appendix).

The collected VNIR, SWIR, and TIR spectral signatures were processed using the commercial software ‘The Spectral Geologist’ (TSG). Mineral abundance and composition information are extracted using the multiple feature extraction method (Cudahy et al., 2008; Laukamp et al., 2010). Positions and depths of absorption features in this study were calculated by locally removing the hull from the reflectance spectra to reduce the influence of instrument or atmospheric noise (Cudahy et al., 2008).

Reflectance spectral geoscience products that are potentially useful for the study of BIF-hosted iron ore include: 1) opaque minerals (e.g. magnetite and pyrite); 2) ferric oxide minerals (e.g. hematite and goethite); 3) kaolinite composition (e.g. crystalline vs poorly crystalline); 4) white micas (e.g. muscovite and phengite); 5) ferrous iron and magnesium bearing sheet silicates (e.g. actinolite and chlorite); 6) carbonate minerals (e.g. calcite, dolomite, and magnesite) (Duuring and Laukamp, 2016a). In all provided examples of reflectance spectral data products, the relative abundance of minerals is indicated by the distribution of the data with vertical depth down the drillhole. The horizontal axes for these plots are without units and show the relative abundance of data. In most plots, the mineral abundance data are coloured on the basis of mineral composition.

## Rock types

BIF is best distinguished from basaltic rocks using the ‘ferric oxide abundance’ spectral product, which detects the combined abundance of hematite and goethite (Fig. 4). In contrast, the ‘opaque mineral abundance’ spectral product, which serves as a proxy for magnetite and sulfides, does not clearly distinguish BIF from mafic rocks (despite this spectral product being effective in the Beebyn WRRD0583 drillhole; Duuring and Laukamp, 2016a) (Fig. 4). It is unclear if the opaque mineral abundance product is influenced by the addition of exotic,

black, fine-grained basalt drillcore to some sample trays prior to scanning with the HyLogger-3 (added for the purpose of filling gaps in drillcore trays). The influence of these exotic intervals has mostly been removed from the processed spectral data, but in several cases they coincide with apparent high abundances of opaque minerals. In addition, dark chlorite-coated fracture planes in mafic igneous rocks appear to correspond at least locally to detected occurrences of opaque minerals. A further effect on the detected abundances of opaque minerals in mafic rocks is that carbonate spectra can increase the overall albedo of BIF intervals, resulting in apparent higher values for the opaque mineral abundance product.

The ‘quartz abundance’ index is generally lower for BIF than mafic igneous rocks (Fig. 4), due to the absence of quartz-rich bands in intensely altered BIF. However, jaspilite displays a similar quartz abundance signature to mafic rocks. Thus, this index depends on hypogene alteration intensity in BIF.

Basaltic rocks universally have higher ‘chlorite’ and ‘chlorite–epidote’ abundance values compared with BIF. More locally, these mafic igneous rocks display elevated values for ‘amphibole–talc’, ‘amphibole’, ‘plagioclase’, ‘serpentine’, and ‘epidote’ abundances (Fig. 4). However, these values vary depending on the local effects of weathering, hypogene alteration, and differences in protolith compositions (e.g. as shown by weathered zones in the Beebyn drillhole; Duuring and Laukamp, 2016a).

Basaltic units that surround the BIF macrobands cannot easily be distinguished from one another based on their petrological characteristics. Instead, immobile element ratios ( $\text{Al}_2\text{O}_3$  vs  $\text{TiO}_2$ ) from bulk-rock geochemical analysis were used to divide these units into different compositional groups that reflect their protolith chemistry (Fig. 5). Mafic1, Mafic4, and Mafic5 units have distinctly different immobile element ratios, with some overlap. In contrast, Mafic2 and Mafic3 intervals have identical  $\text{Al}_2\text{O}_3$  vs  $\text{TiO}_2$  ratios. The geochemical data suggest that the mafic intervals represent a series of extrusive lava flows with different compositions. The comparable ratios demonstrated by the Mafic2 and Mafic3 intervals indicate that they are likely to be the same unit that has been repeated due to fault displacement. The large compositional spread in Mafic1 data suggests that this interval comprises multiple, discrete subunits, assuming that  $\text{Al}_2\text{O}_3$  vs  $\text{TiO}_2$  ratios were not significantly disturbed by hydrothermal alteration.

The Mafic1 and Mafic4 intervals have the highest detected abundances of amphibole compared with other basalt units in the drillhole (Fig. 4). Fe/Mg ratios for these amphiboles mostly range between the Fe- and Mg-rich end member compositions for amphibole.

## Hypogene alteration zones in BIF

Relative to least-altered jaspilitic BIF, the intensely hypogene-altered BIF displays a higher opaque mineral abundance signature (Fig. 6a) but a lower quartz abundance index (Fig. 6b). These spectral products accurately mirror observed enrichments in primary and



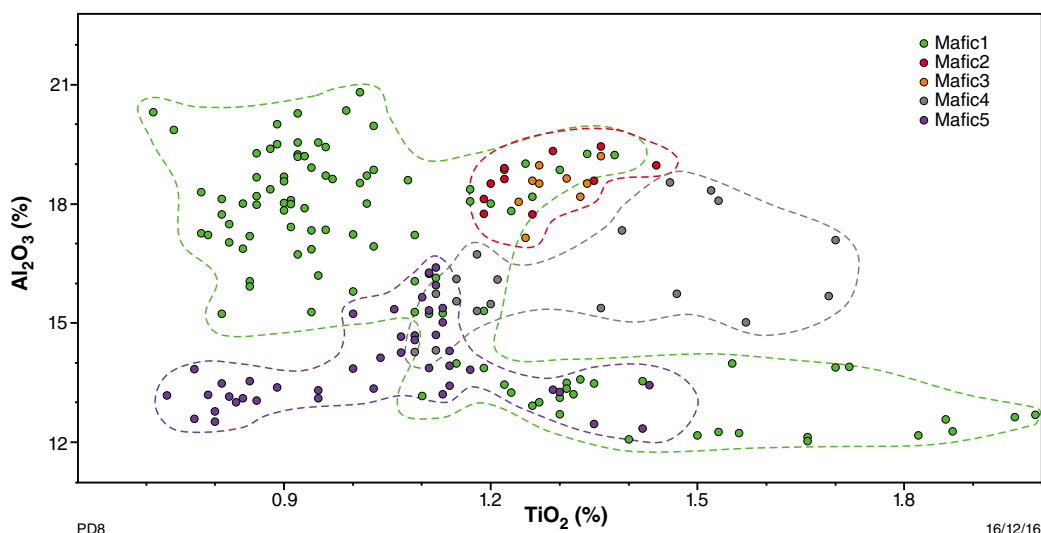


**Figure 5. Primary compositional differences in basalt units (Mafic1 to Mafic5 intervals). Immobile elements from bulk-rock geochemical data ( $\text{Al}_2\text{O}_3$  vs  $\text{TiO}_2$ ) for mafic igneous rocks demonstrate variations between most intervals, with the exception of overlapping ratios for Mafic2 and Mafic3 intervals.**

hypogene magnetite, and corresponding depletion of primary quartz bands in high-grade iron ore zones. In addition, the ferric oxide abundance product illustrates the effects of later hypogene hematite–chlorite alteration (Fig. 6c) and possibly the local presence of weak supergene goethite–hematite alteration in BIF.

High-grade iron ore zones hosted by BIF contain minor hydrothermal chlorite (Fig. 7). In these areas, hypogene-altered BIF with magnetite–carbonate is further altered to specularite–chlorite. These high-grade iron ore zones display chlorite with the highest  $\text{Fe}_{\text{total}}$  content of all rocks intersected by the drillhole. In contrast, chlorites hosted by BIF outside the high-grade ore zones display a range in compositions from Fe rich to Mg rich (Fig. 4).

Hypogene carbonate is present in BIF primarily as dolomite, with minor magnesite or siderite (Fig. 4). Dolomite and magnesite occurrences correspond to observed late-stage dolomite veins and breccias that cut hypogene magnetite-altered BIF, whereas the carbonate in BIF1 is most likely siderite (Fig. 4).

## Hypogene alteration zones in mafic igneous rocks

Basaltic units proximal to BIF macrobands are enriched in chlorite and depleted in amphibole compared with distal zones (Fig. 4). Furthermore, hypogene chlorite in mafic rocks becomes increasingly Fe enriched with proximity to BIF-hosted hypogene iron ore zones. For example, the Mafic1 and Mafic2 proximal zones display the most pronounced enrichments in Fe-chlorite of all wallrocks to BIF macrobands (Fig. 8a,b). The corresponding BIF macrobands (BIF1 and BIF2) display the most intense and pervasive hypogene alteration of all intersected BIF.

Mg-rich chlorite is more likely to be hosted by basaltic rocks in distal areas (Fig. 4). However, some intervals of mafic igneous rocks, such as the Mafic4 interval, do not show pronounced differences in chlorite composition despite the greater abundance of chlorite detected in proximal alteration zones (Fig. 8c).

Carbonate minerals were detected by the SWIR and TIR spectrometers in particular intervals from all mafic igneous rocks in the drillhole (e.g. 360–372 m in Fig. 4). The TIR spectra for these carbonate minerals indicate varying combinations of Fe and Mg abundance, compatible with the presence of dolomite to ferroan dolomite. Leucoxene was identified by conventional logging as an important indicator mineral for distal alteration zones, whereas its absence indicated the presence of proximal alteration zones. Leucoxene was likely to have been too fine grained to be resolved in the mixed spectra.

## Supergene alteration zones in BIF

Supergene alteration is negligible in BIF, although the presence of minor kaolinite throughout the BIF – mafic rock intervals (310–384 m) is most likely related to weak supergene alteration (Fig. 4).

## Supergene alteration of mafic igneous rocks

Weak to moderate supergene alteration is exhibited by basaltic rocks from about 245 to 265 m. In these areas, primary igneous amphibole and plagioclase, and metamorphic or hypogene chlorite, display an inverse relationship relative to the abundance of detected kaolinite (Fig. 4).

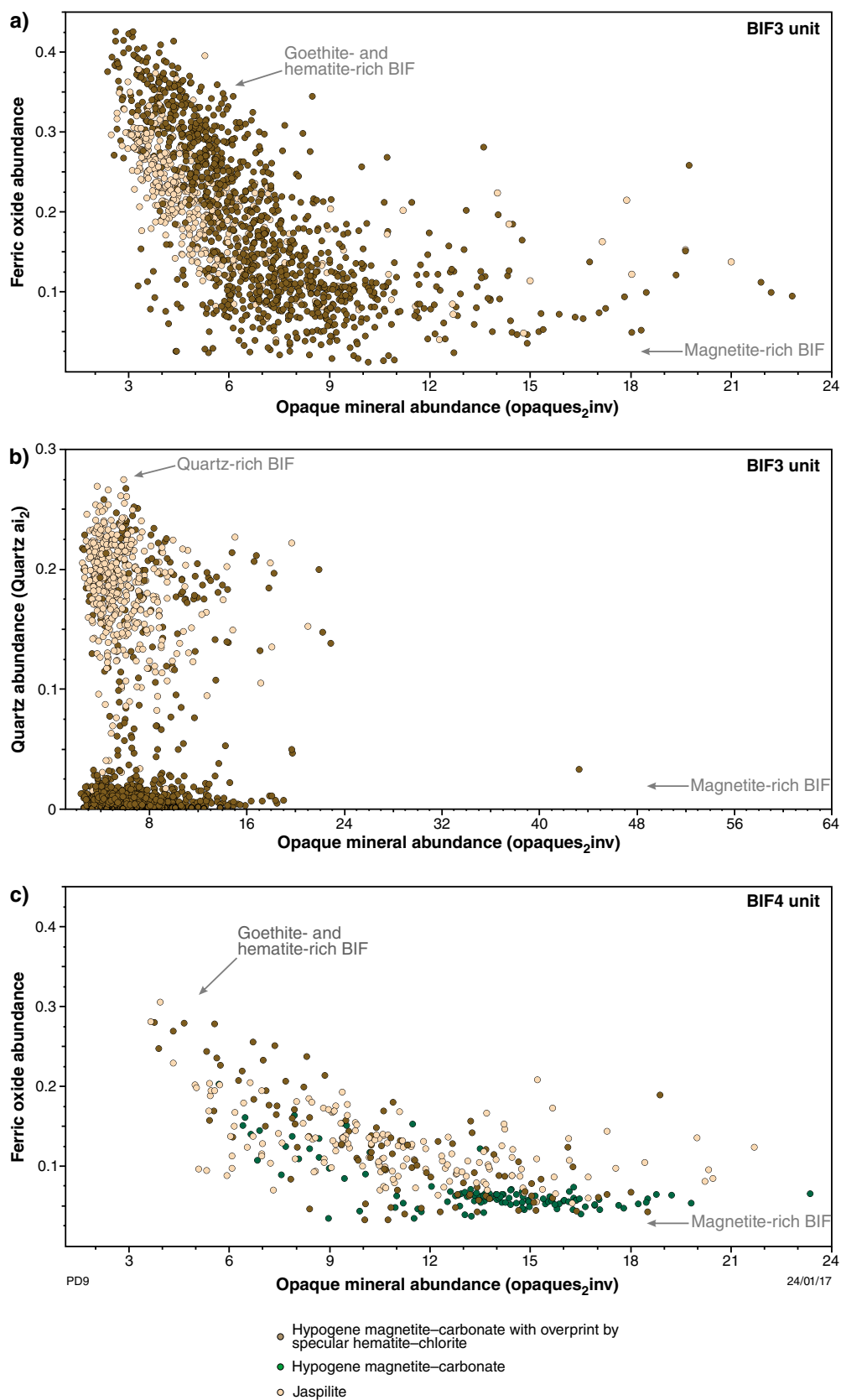


**Figure 6.** Scatter plots of hyperspectral data for BIF: a) abundance of ferric oxide species (hematite and goethite) vs opaque mineral abundance (magnetite) for jaspilite and high-grade iron ore in BIF3; b) quartz abundance vs opaque mineral abundance for the same BIF3 unit; c) ferric oxide abundance vs opaque minerals in BIF4. Relative to jaspilite, high-grade iron ore zones generally contain more opaque minerals and are depleted in quartz. High-grade iron ore zones display an inverse relationship between hematite+goethite and magnetite.

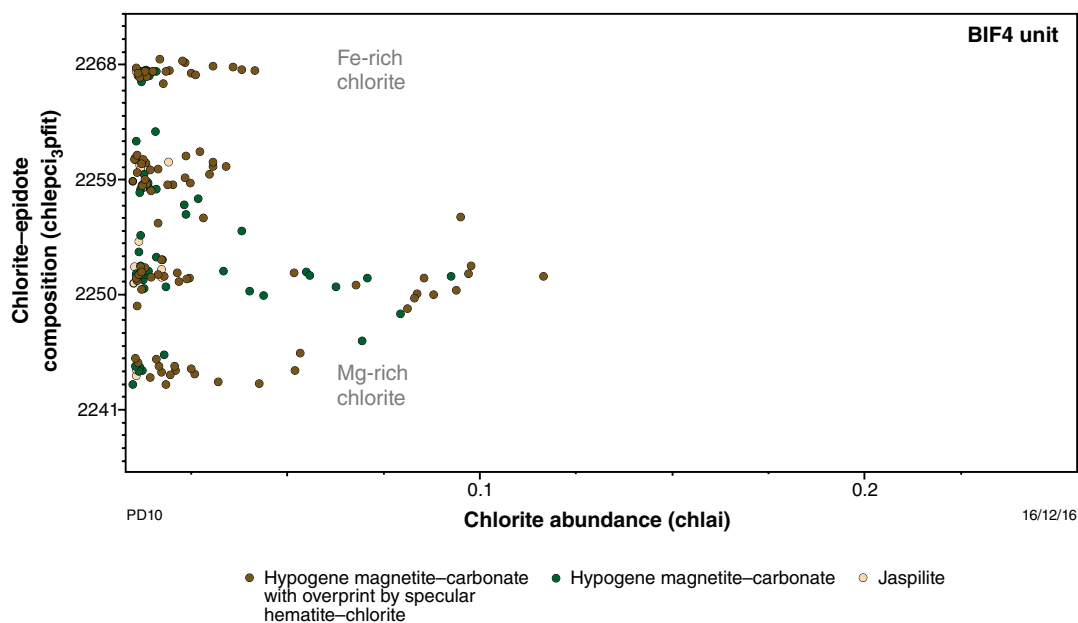


**Figure 7. Chlorite Fe/Mg compositional variations in the BIF4 interval. Within this macroband, jaspilite and high-grade iron ore all display a large variation in chlorite chemistry, with Fe-rich, Fe-Mg, and Mg-rich varieties locally present.**

## Conclusions

Core from diamond drillhole W2DDH007, located in the W2 deposit of the Windarling iron camp, was scanned by the HyLogger-3 at GSWA's Perth Core library. The hyperspectral data were compared with data collected from the conventional logging of the drillhole. Hyperspectral data accurately distinguish rock types, mineral abundance, and mineral chemistry at a resolution of about 1 cm continuously down the drillhole.

BIF is best distinguished from mafic igneous rocks using the ferric oxide abundance spectral product, which detects the combined abundance of hematite and goethite in rocks. This method is an effective discriminator of unweathered rocks only and is less accurate in supergene-altered rocks (as demonstrated by the study of the Beebyn drillhole WRRD0583; Duuring and Laukamp, 2016a). Surprisingly, the opaque mineral abundance spectral product does not accurately distinguish BIF from mafic igneous rocks (despite this spectral product being effective in the Beebyn WRRD0583 drillhole). Several parameters may have influenced its effectiveness: 1) the ineffective masking of segments of exotic black fine-grained basalt drillcore that were added for the purpose of filling gaps in the highly reflective sample trays; 2) the presence of dark chlorite-covered fracture planes in mafic igneous rocks; 3) the presence of carbonate minerals whose spectra may increase the overall albedo of BIF intervals.

Basaltic rocks universally display higher chlorite and chlorite-epidote abundance signatures compared with

BIF. More locally, these mafic igneous rocks display elevated signatures for amphibole-talc, amphibole, plagioclase, serpentine, and epidote abundances; however, these signatures vary depending on the local effects of weathering, hypogene alteration, and differences in protolith compositions.

High-grade iron ore zones hosted by BIF show a major decrease in the quartz abundance index that is related to the dissolution of quartz bands from these rocks by hydrothermal fluids. Disseminated siderite is locally preserved in the hypogene magnetite-bearing zones, where it likely replaces primary quartz bands. Later dolomite veins and breccias appear to cut hypogene magnetite ± siderite-altered BIF.

Hypogene magnetite ± carbonate-altered BIF that displays a specularite-chlorite overprint has a high ferric oxide abundance signature. Chlorite abundance is low in BIF; where present, the chlorite composition varies from Fe rich to Mg rich.

Mafic igneous rocks located proximal to BIF macrobands are enriched in chlorite and depleted in amphibole relative to more distal zones. In addition, hypogene chlorite becomes increasingly Fe rich with proximity to BIF-hosted hypogene iron ore zones. BIF1 and BIF2 are surrounded by the most pronounced Fe-chlorite alteration haloes in mafic igneous wall rocks, most likely because these BIF macrobands are the most intensely and pervasively altered by hypogene fluids.

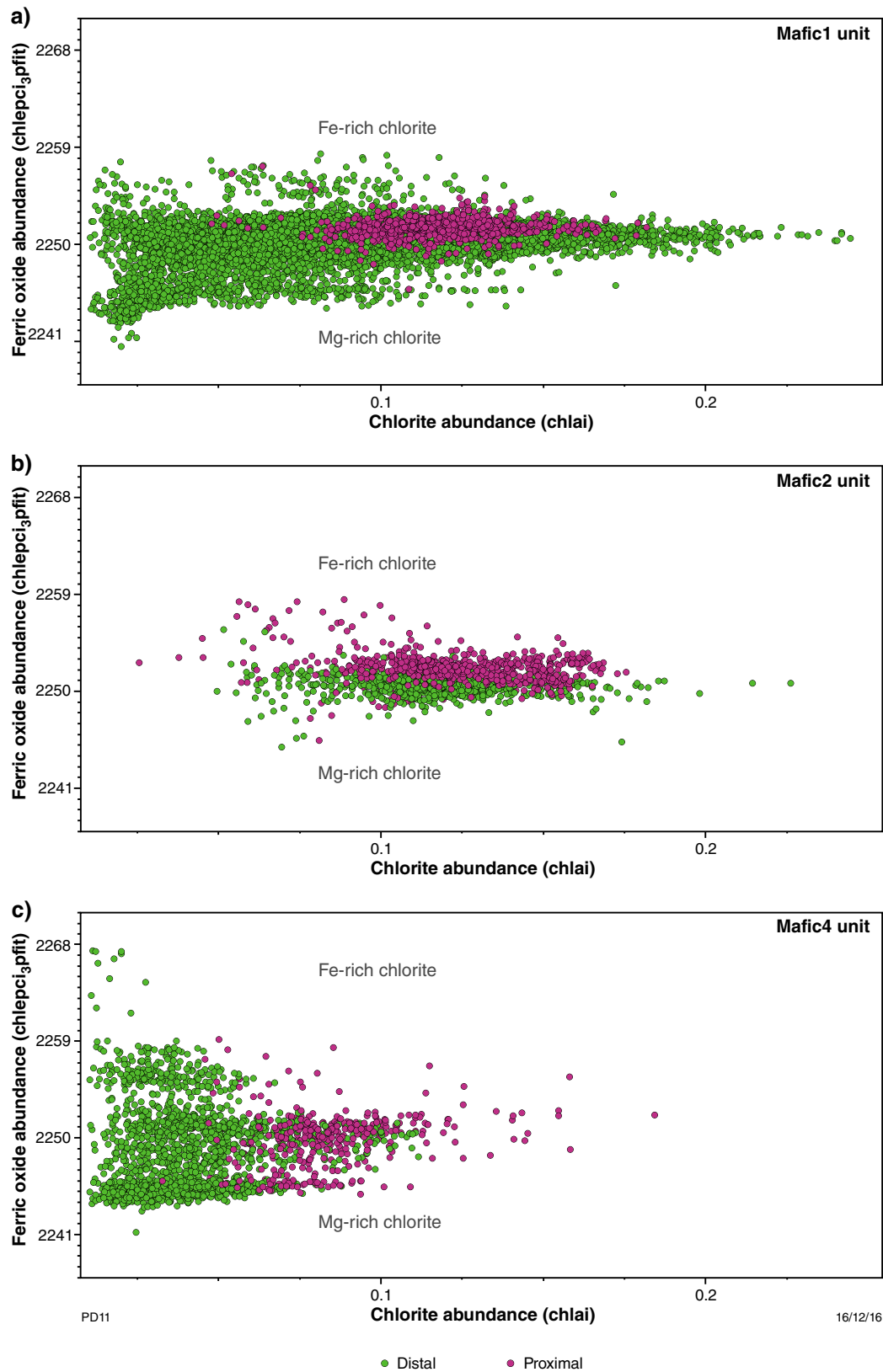


**Figure 8.** A comparison of chlorite chemistry for proximal and distal alteration zones in mafic igneous rocks: a) Mafic1; b) Mafic2; c) Mafic4. For Mafic1 and Mafic2, chlorite in the proximal alteration zones is comparatively enriched in Fe relative to the more distal zones. However, the Mafic4 interval displays chlorite with similar Fe/Mg ratios.

## Acknowledgements

This study was funded by the Geological Survey of Western Australia's Exploration Incentive Scheme (a Royalties for Regions initiative). We thank Cliffs Natural Resources for providing access to drillhole W2DDH007.

## References

- Angerer, T, Hagemann, SG and Danyushevsky, L 2013, High-grade iron ore at Windarling, Yilgarn craton: a product of syn-orogenic deformation, hydrothermal alteration, and supergene modification in an Archean BIF–basalt lithostratigraphy: *Mineralium Deposita*, v. 48, p. 697–728.
- Bishop, JL, Lane, MD, Dyar, MD and Brown, AJ 2008, Reflectance and emission spectroscopy study of four groups of phyllosilicates: smectites, kaolinite-serpentines, chlorites and micas: *Clay Minerals*, v. 43, p. 35–54.
- Cassidy, KF, Champion, DC, Krapež, B, Barley, ME, Brown, SJA, Blewett, RS, Groenewald, PB and Tyler, IM 2006, A revised geological framework for the Yilgarn Craton, Western Australia: Geological Survey of Western Australia, Record 2006/8, 8p.
- Clark, RN and Roush, TL 1984, Reflectance spectroscopy: Quantitative analysis techniques for remote sensing applications: *Journal of Geophysical Research: Solid Earth*, v. 89, no. B7, p. 6329–6340.
- Cudahy, TJ, Jones, M, Thomas, M, Laukamp, C, Caccetta, M, Hewson, RD, Rodger, AR and Verrall, M 2008, Next generation mineral mapping: Queensland airborne HyMap and satellite ASTER surveys 2006–2008: CSIRO, Open File Report P2007/364, 120p.
- Duke, E 1994, Near infrared spectra of muscovite, Tschermak substitution, and metamorphic reaction progress: Implications for remote sensing: *Geology*, v. 22, p. 621–624.
- Duuring, P and Laukamp, C 2016a, Mapping iron ore alteration patterns in banded iron-formation using hyperspectral data: Beebyn deposit, Yilgarn Craton, Western Australia: Geological Survey of Western Australia, Record 2016/16, 18p.
- Duuring, P and Laukamp, C 2016b, Mapping iron ore alteration patterns in banded iron-formation using hyperspectral data: drillhole PK11DD001, Mt Richardson, Yilgarn Craton, Western Australia: Geological Survey of Western Australia, Record 2016/18, 15p.
- Duuring, P and Laukamp, C 2016c, Mapping iron ore alteration patterns in banded iron-formation using hyperspectral data: drillhole PK12DD001, Mt Richardson, Yilgarn Craton, Western Australia: Geological Survey of Western Australia, Record 2016/19, 19p.
- Geological Survey of Western Australia 2016, 1:500 000 State interpreted geology of Western Australia, 2016: Geological Survey of Western Australia, digital data layer, <www.dmp.wa.gov.au/geoview>.
- Haest, M, Cudahy, T, Laukamp, C and Gregory, S 2012a, Quantitative mineralogy from infrared spectroscopic data. (I) Validation of mineral abundance and composition scripts at the Rocklea channel iron deposit in Western Australia: *Economic Geology*, v. 107, no. 2, p. 209–228.
- Haest, M, Cudahy, T, Laukamp, C and Gregory, S 2012b, Quantitative mineralogy from visible to shortwave infrared spectroscopic data. (II) Three-dimensional mineralogical characterisation of the Rocklea channel iron deposit, Western Australia: *Economic Geology*, v. 107, no. 2, p. 229–249.
- Hancock, EA, Green, AA, Huntington, JF, Schodlok, MC and Whitbourn, LB 2013, HyLogger-3: Implications of adding thermal-infrared sensing: Geological Survey of Western Australia, Record 2013/3, 24p.
- Hunt, G 1977, Spectral signatures of particular minerals in the visible and near infrared: *Geophysics*, v. 42, no. 3, p. 501–513, doi:10.1190/1.1440721.
- Laukamp, C 2011, Short wave infrared functional groups of rock-forming minerals: CSIRO, Report EP115222, 13p.
- Laukamp, C, Caccetta, M, Chia, J, Cudahy, T, Gessner, K, Haest, M, Liu, YC, Ong, C and Rodger, A 2010, The uses, abuses and opportunities for hyperspectral technologies and derived geoscience information: AIG Bulletin; Geo-Computing 2010 Conference, Brisbane, September 2010, no. 51, p. 73–76.
- Laukamp, C, Termin, KA, Pejčić, B, Haest, M and Cudahy, T 2012, Vibrational spectroscopy of calcic amphiboles — applications for exploration and mining: *European Journal of Mineralogy*, v. 24, p. 863–878.
- Sonntag, I, Laukamp, C and Hagemann, SG 2012, Low potassium hydrothermal alteration in low sulfidation epithermal systems as detected by IRS and XRD: An example from the Co-O mine, Eastern Mindanao, Philippines: *Ore Geology Reviews*, v. 45, p. 47–60.

Appendix

Description of spectral scripts for geoscience products

Product name	Minerals detected	Base algorithm	Filters/Masks	Lower stretch limit	Upper stretch limit (based on UGD1683)	Related publication	Comments on general accuracy
Opaques abundance	Sulfides, carbon black (e.g. ash, magnetite, or Mn oxides)	(R456)/(R1650) OPAQUES_450D1650	albedo @ 1650 nm <30%	0.25: low content	Not specified yet – depending on results from other drillcores		Moderate: errors introduced by a lack of Fe <sup>3+</sup> absorption in the visible, e.g. iron oxide poor clays that, in theory, would be masked by the <30% albedo but may be in partial 'shadow'
Ferric oxide abundance (Ferric_oxide_abundance.txt)	Hematite, goethite, jarosite	Continuum removed depth of the 900 nm absorption calculated using a fitted 2nd order polynomial between 776 and 1050 nm. 900D	R450 > R1650	0.04: low content	Not specified – depending on whole dataset	Further developed on the basis of Haest et al. (2012a,b), which used a 4th order polynomial or 4 band ratio approach	Low at Stavely: compromised by other tranistion metal-bearing minerals (e.g. pyroxene). High in regolith and iron ore deposits (Rocklea case study: RMSE = 9.7%)
hem/goe (Hematite-goethite.txt)	Hematite/goethite ratio	Continuum removed wavelength of the 900 nm absorption minimum calculated using a fitted 12th order polynomial between 776 and 1150nm. 900W	R450 > R1650 + 900D >0.025	~900 nm: more hematitic	~940 nm: more goethitic	Haest et al. (2012a,b)	Moderate: wavelength accuracy of the iron-oxide crystal field absorption is adversely affected by mixing with green and dry vegetation as well as ferrous-bearing carbonate and silicate minerals
Kaolin abundance (Kaolin_abundance_2011v2.txt)	Kaolin group minerals: kaolinite halloysite, dickite and nacrite	2200D (Normalized depth of a fitted 4th order polynomial between 2120 and 2245 nm)	2160D [(R2138+R2190)/(R2156+R2179)] >1.005	0.04: low content	Not specified – depending on whole dataset	Sonntag et al. (2012)	High in regolith, low in low-metamorphic grade rocks: compromised by pyrophyllite and prehnite
Kaolin composition (Kaolin_comp_2011v2.txt)	Composition and crystallinity of kaolin group minerals ranging from well-ordered kaolinite to halloysite to dickite (and nacrite)	[(R2138+R2173/R2156)]/[(R2156+R2190)/R2173]	2200D>0.005	Not specified yet – depending on results from other drillcores	Not specified – depending on whole dataset	Sonntag et al. (2012)	Moderate, but compromised by pyrophyllite and prehnite
White mica abundance (wmAlsmat.txt)	Abundance of white micas (e.g. illite, muscovite, paragonite, brammalite, phengite, lepidolite, margarite) and smectites (montmorillonite, beidellite)	Relative absorption depth of the 2200 nm absorption for which the continuum is removed between 2120 and 2245, determined using a 3 band polynomial fit around the band with the lowest reflectance. 2200D3pfit	(R2326+R2376)/(R2343 + R2359) 2350DE >0.00035) + ((R2138+R2190)/(R2156 + R2179) 2160D2190 <1.063	0.04: low content	Not specified – depending on whole dataset	Further developed on the basis of Sonntag et al. (2012), which used a 4th order polynomial or 4 band ratio approach	Moderate: inherent errors related to the process of masking rather than unmixing. That is, the threshold levels on mask parameters could exclude or include other materials especially for 'lower' levels. In sedimentary rocks at Stavely, problems with overlapping kaolinite
White mica composition (wmAlsmci.txt)	Tschermak substitution of white micas, ranging from paragonite, brammalite, to illite, muscovite to phengite, and smectites, ranging from beidellite to montmorillonite	Minimum wavelength of the 2200 nm absorption for which the continuum is removed between 2120 and 2245, determined using a 3 band polynomial fit around the band with the lowest reflectance. 2200W3pfit	(R2326+R2376)/(R2343 + R2359) 2350DE >0.00035) + ((R2138+R2190)/(R2156 + R2179) 2160D2190 <1.063	2185 nm: Al-rich mica (muscovite, illite, paragonite, brammalite, lepidolite)	2220 nm: Al-poor mica (~phengite)	Further developed on the basis of Sonntag et al. (2012), which used a 4th order polynomial or 4 band ratio approach	High: internationally established parameter for tracking Tschermak exchange in white micas and Al-smectites (e.g. Duke, 1994)
Chlorite–epidote abundance (chlepai3pfit.txt)	Chlorite, epidote, biotite	Relative absorption depth of the 2250 nm absorption for which the continuum is removed between 2230 and 2270, determined using a 3 band polynomial fit around the band with the lowest reflectance. 2250D3pfit	2250D3pfit >0.01, 2230 nm < 2250W < 2270 nm	0.04: low content	Not specified – depending on whole dataset	Further developed on the basis of Sonntag et al. (2012), which used a 4th order polynomial or 4 band ratio approach	Moderate: can be influenced by abundant jarosite, tourmaline, phlogopite. Probably some correlation with ferrous iron abundance
Chlorite–epidote composition (chlepci3pfit.txt)	Chlorite, epidote, biotite	Relative absorption depth of the 2250 nm absorption for which the continuum is removed between 2230 and 2270, determined using a 3 band polynomial fit around the band with the lowest reflectance. 2250D3pfit	2250D3pfit >0.01, 2230 nm < 2250W < 2270 nm	2248 nm: Mg-rich (Bishop et al., 2008)	2261 nm: Fe-rich (Bishop et al., 2008)	Further developed on the basis of Sonntag et al. (2012), which used a 4th order polynomial or 4 band ratio approach	Moderate: can be influenced by abundant jarosite, tourmaline, phlogopite. Probably some correlation with ferrous iron abundance
Carbonate abundance index TIR (6500P_3pfit.txt)	Calcite, dolomite, magnesite, siderite, ankerite	6500P Relative height of the reflectance peak between 6300 and 6700 nm, determined using a 3 band polynomial fit around the band with the highest reflectance		0.1	Not specified – depending on whole dataset	Inherited, unpublished	High, but lower threshold dependent on dataset
Carbonate composition index TIR1 (14000DW_3pfit.txt)	Calcite, dolomite, magnesite, siderite, ankerite	14000DW Minimum wavelength of the reflectance low between 13000 and 14000 nm, determined using a 3 band polynomial fit around the band with the lowest reflectance		13000 nm: Mg/Fe-rich	14000 nm: Ca-rich	Inherited, unpublished	High, but lower threshold dependent on dataset
Carbonate abundance (Carbonate_abundance_SWIR.txt)	Carbonates vs MgOH-bearing silicates, based on left-asymmetry of CO <sub>3</sub> feature @ 2340	Relative absorption depth of the 2340 nm absorption for which the continuum is removed between 2270 and 2370, determined using a 3 band polynomial fit around the band with the lowest reflectance. 2340D	2340D >0.04, 2295 nm < 2340W < 2360 nm, 2250D < 0.025, 2380D < 0.1117*2340D + 0.0002. Asymmetry of the 2340 absorption using a fitted 4th order polynomial between 2120 and 2370: 2340_left_asym > 1.13	0.05: low content	Not specified – depending on whole dataset	Further developed on the basis of Sonntag et al. (2012), which used a 4th order polynomial or 4 band ratio approach	Low: heavily impacted by grain size effects. False positives in case of mineral mixtures of, for example, white mica and chlorite
Carbonate composition SWIR (Carbonate_composition_SWIR.txt)	Separating calcite, dolomite, and siderite	Minimum wavelength of the 2340 nm absorption for which the continuum is removed between 2270 and 2370, determined using a 3 band polynomial fit around the band with the lowest reflectance. 2340W	2340D >0.04, 2295 nm < 2340W < 2360 nm, 2250D < 0.025, 2380D < 0.1117*2340D+0.0002. Asymmetry of the 2340 absorption using a fitted 4th order polynomial between 2120 and 2370: 2340_left_asym > 1.13	2303 nm: magnesite; 2326 nm: dolomite; recommendation for Stavely dataset: 2320 nm	2343 nm: calcite; recommendation for Stavely dataset: 2320 nm	Further developed on the basis of Sonntag et al. (2012), which used a 4th order polynomial or 4 band ratio approach	Moderate: works well for those carbonates, which are not masked out by the carbonate abundance index SWIR, The latter should be replaced by carbonate abundance index TIR
Amphibole–talc abundance (Amph_Talc_abundance.txt)	Abundance of amphibole and talc	2380D [(R2365+R2415)/(R2381+R2390)]	Composite mask* + MgOH abundance > 1.01 (+ 2160D2190 < 1.005)	1.005: low content	Not specified – depending on whole dataset	Laukamp et al. (2012)	Moderate: can be compromised by abundant phlogopite; noise
2080D3 (2080D3pfit.txt)	Depth of the 2080 feature, evident in talc. Useful for separating talc from amphiboles, the latter in general not showing this absorption feature	Depth of the 2080 nm absorption feature, for which the continuum is removed between 2060 and 2100, determined using a second order polynomial fitted through the 3 bands with the lowest reflectance. 2080D				Laukamp et al. (2012)	
2390W (2390W3pfit.txt)	Estimate of the Mg/Fe ratio (Mg#) in, for example, amphiboles and talc	Wavelength of absorption minimum calculated using a fitted fourth order polynomial between 2365 and 2430 nm, focused between 2380 and 2410 nm. 2390W		2382 nm: Mg-rich (Laukamp et al., 2012)	2406 nm: Fe-rich (Laukamp et al., 2012)	Laukamp et al. (2012)	
Quartz abundance	Quartz	8635D Relative depth of the 8626 nm Reststrahlen feature for which the continuum is removed between 8565 and 8705 nm, determined using a 3 band polynomial fit around the band with the lowest reflectance	no mask	0.1	Not specified – depending on whole dataset	Inherited, unpublished	High, but lower threshold dependent on dataset. Fractured drillcore can lead to extreme overestimation

References:

Bishop, J.L, Lane, MD, Dyar, MD and Brown, AJ 2008, Reflectance and emission spectroscopy study of four groups of phyllosilicates: smectites, kaolinite-serpentines, chlorites and micas: Clay Minerals, v. 43, p. 35–54

Duke, E 1994, Near infrared spectra of muscovite, Tschermak substitution, and metamorphic reaction progress: Implications for remote sensing: Geology, v. 22, p. 621–624.

Haest, M, Cudahy, T, Laukamp, C and Gregory, S 2012a, Quantitative mineralogy from visible to shortwave infrared spectroscopic data. (I) Validation of mineral abundance and composition products of the Rocklea Dome channel iron deposit in Western Australia: Economic Geology, v. 107, p. 209–228.

Haest, M, Cudahy, T, Laukamp, C and Gregory, S 2012b, Quantitative mineralogy from visible to shortwave infrared spectroscopic data. (II) Three-dimensional mineralogical characterisation of the Rocklea Dome channel iron deposit, Western Australia: Economic Geology, v. 107, p. 229–249.

Laukamp, C, Termin, KA, Pejic, B, Haest, M and Cudahy, T 2012, Vibrational spectroscopy of calcic amphiboles – applications for exploration and mining: European Journal of Mineralogy, v. 24, p. 863–878.

Sonntag, I, Laukamp, C and Hagemann, S 2012, Low potassium hydrothermal alteration in low sulfidation epithermal systems as detected by IRS and XRD: an example from the Co-O Mine, Eastern Mindanao, Philippines: Ore Geology Reviews, v. 45, p. 47–60.



MAPPING IRON ORE ALTERATION PATTERNS IN BANDED  
IRON-FORMATION USING HYPERSPECTRAL DATA:  
WINDARLING IRON CAMP, YILGARN CRATON, WESTERN AUSTRALIA

This Record is published in digital format (PDF) and is available as a free download from the DMP website at  
<[www.dmp.wa.gov.au/GSWApublications](http://www.dmp.wa.gov.au/GSWApublications)>.

Further details of geological products produced by the  
Geological Survey of Western Australia can be obtained by contacting:

Information Centre  
Department of Mines and Petroleum  
100 Plain Street  
EAST PERTH WESTERN AUSTRALIA 6004  
Phone: +61 8 9222 3459 Fax: +61 8 9222 3444  
[www.dmp.wa.gov.au/GSWApublications](http://www.dmp.wa.gov.au/GSWApublications)

